Dalton Transactions

PAPER

View Article Online
View Journal | View Issue

Cite this: *Dalton Trans.*, 2018, **47**, 1223

Influence of the manganese and cobalt content on the electrochemical performance of P2-$Na_{0.67}Mn_xCo_{1-x}O_2$ cathodes for sodium-ion batteries†

K. Hemalatha,‡[a,b] M. Jayakumar ‡[a,c] and A. S. Prakash *[a,b]

Received 20th November 2017,
Accepted 13th December 2017

DOI: 10.1039/c7dt04372d

rsc.li/dalton

The resurgence of sodium-ion batteries in recent years is due to their potential ability to form intercalation compounds possessing a high specific capacity and energy density comparable to existing lithium systems. To comprehend the role of cobalt substitution in the structure and electrochemical performance of $Na_{0.67}MnO_2$, the solid solutions of P2-$Na_{0.67}Mn_xCo_{1-x}O_2$ (x = 0.25, 0.5, 0.75) are synthesized and characterized. The XRD-Rietveld analysis revealed that the Co-substitution in $Na_{0.67}MnO_2$ decreases lattice parameters '*a*' and '*c*' resulting in the contraction of MO_6 octahedra and the enlargement of interlayer '*d*' spacing. XPS indicates that the isovalent cobalt substitution in $Na_{0.67}MnO_2$ results in the partial/complete replacement of Jahn–Teller active trivalent manganese to form low-spin complexes of better structural stability. The Na-ion diffusion coefficient, D_{Na^+}, derived from cyclic voltammetry and impedance spectroscopy, confirmed the enhanced mass transport in Co-rich phases compared to Mn-rich phases. Furthermore, higher diffusion coefficient values are observed for Co^{3+}/Co^{4+} than for their Mn^{3+}/Mn^{4+} redox processes. In addition, Co-rich phases exhibit a high structural stability and superior capacity retention, whereas Mn-rich phases discharge higher capacities.

1. Introduction

Rechargeable sodium-ion batteries are among the front-runners in the pursuit of energy storage systems beyond Li-ion batteries.[1,2] Sodium-based energy storage overcomes the issues related to cost and scanty resources of lithium. Sodium storage systems are attractive for niché applications such as stationary grid storage which require inexpensive, safe and long life solutions while offering flexibility in terms of energy density.[3–6] Although electrochemistry and the insertion mechanism are similar in both batteries, only recent years have witnessed sodium-ion batteries catching up with Li-ion batteries due to regained research interest and the realization of Na-insertion electrodes with capacities comparable to commercialized Li-ion cathodes.[7–10]

Among various sodium compounds classified on the basis of the crystal structure, 2D sodium lamellar oxides of the generic formula Na_xMO_2 are widely investigated as cathode materials due to their structure and high specific capacity.[11,12] P2-type Na_xMO_2 compounds exhibit a higher capacity and superior rate performance than O3 phases, due to their better structural stability and different Na-ion diffusion pathways.[13–17] In P2-type compounds, the unit cell contains two MO_2 layers with edge sharing MO_6 octahedra, while Na-ion exists in the prismatic (P) site.[18] Among the P2 phases, Na_xMnO_2 enjoy academic and commercial interest as they intercalate higher sodium per formula unit due to their superior structural flexibility.[19–23]

P2-type $Na_{0.67}MnO_2$ contains two MnO_6 octahedra with Na^+ in a trigonal prismatic environment. In this compound, nearly two-thirds of manganese exist in the +3 oxidation state and the remaining one-third oxidizes to +4 to compensate the deficient sodium.[24,25] The presence of Jahn–Teller high spin Mn^{3+} ions reduces the diffusion coefficient of sodium and destabilizes the structure.[21] Also, during sodiation/desodiation, the P2 $Na_{0.67}MnO_2$ phase irreversibly transforms to the O2 phase with multiple potential plateaus resulting in notable capacity losses.[22] Partial substitution of manganese with other electro-

[a]*CSIR-Central Electrochemical Research Institute-Chennai Unit, CSIR Madras Complex, Taramani, Chennai 600113, India. E-mail: prakash@cecri.res.in, prakash.as@gmail.com*
[b]*Academy of Scientific and Innovative Research (AcSIR), CSIR-Central Electrochemical Research Institute-Chennai Unit, CSIR Madras Complex, Chennai 600113, India*
[c]*Electroplating and Metal Finishing Division, CSIR-Central Electrochemical Research Institute, Karaikudi 630006, India*

† Electronic supplementary information (ESI) available: XRD, SEM, analysis of cyclic voltammetry and electrochemical impedance spectroscopy data, and summary of the literature on P2-$Na_{0.67}Mn_xCo_{1-x}O_2$. See DOI: 10.1039/c7dt04372d

‡ Equally contributing first authors.

chemically active transition metal ions (Ni^{2+}, Co^{3+}, Fe^{3+}, Ti^{4+})[26–30] and electrochemically inactive ions (Li^{+}, Mg^{2+}, Al^{3+})[31–34] favors the oxidation of Mn^{3+} to Mn^{4+}, which is expected to overcome such undesired structural instability and irreversible phase transformation. As a result, such compounds have shown a superior electrochemical performance than the parent compound in terms of capacity retention and rate capability as the Jahn–Teller effect associated with Mn^{3+} ions is suppressed.[26–34]

In particular, cobalt substitution in P2-Na_xMnO_2 is expected to improve the electrode performance as it enhances the electrical conductivity and Na-ion diffusion.[21,35,36] The existing reports on $Na_{2/3}Mn_yCo_{1-y}O_2$ phases focus on improving the electrode performance[27,35–42] by tuning the morphology, composition, and so forth. To the best of our knowledge, the effect of Co-doping in Na_xMnO_2 on Na-ion diffusion and its correlation with the structural stability and electrochemical performance has not been investigated. The prima facie is to estimate D_{Na^+} at specific potentials corresponding to the Co^{3+}/Co^{4+} (above 3 V) or Mn^{3+}/Mn^{4+} (below 3 V) redox. Hence, the diffusion coefficient D_{Na^+} calculated at different redox potentials could offer insights into the mechanistic understanding of the Na-ion transport phenomenon and charge storage properties.

Here we report few compositions of cobalt doped layered sodium manganese oxides, $Na_{0.67}Mn_xCo_{1-x}O_2$ (x = 0.25, 0.5, 0.75), as cathode materials for Na-ion batteries. Using structural analysis, cyclic voltammetry and impedance spectroscopy supported by electrochemical Na-ion storage, we comprehend the positive role of Co doping in the $Na_{0.67}MnO_2$ cathode.

2. Experimental section

2.1 Material preparation

$Na_{0.67}Mn_{0.25}Co_{0.75}O_2$, $Na_{0.67}Mn_{0.5}Co_{0.5}O_2$ and $Na_{0.67}Mn_{0.75}Co_{0.25}O_2$ (henceforth referred to as MC25, MC50 and MC75, respectively) phases were prepared by an urea–glycine assisted combustion method.[43] The stoichiometric amounts of metal nitrate salts of Na, Mn and Co ($0.72 : x : 1 - x$ molar ratio) and mixed fuel (urea and glycine – 3 : 1 molar ratio) were dissolved in a minimum amount of water. In order to compensate the sodium loss occurring at annealing temperature, which is closer to the boiling point of sodium (882.94 °C), about 5% excess of sodium nitrate (with respect to 0.67 moles of Na) was taken during the synthesis. The solution was made homogeneous and introduced into a preheated muffle furnace at 700 °C. The solution boils, froths, and undergoes exothermic flaming combustion to result in a black colored product. The as-prepared powder was reheated in a muffle furnace at 900 °C for 6 h to obtain a carbon free crystalline product. All the samples were then quenched at 300 °C, ground and stored in an argon filled glove box.

2.2 Material characterization

XRD measurements were carried out on well-ground powder samples in a transmission geometry at ambient temperature and pressure using synchrotron facility at Extreme conditions XRD (ECXRD) beamline (BL-11), Indus-2, RRCAT.[44] For this purpose, we used the angle dispersive mode at wavelength λ = 0.5052 Å. A MAR345 imaging plate system was used to collect two-dimensional XRD patterns. The calibration of the X-ray photon energy and the distance between the sample and the image plate was carried out by using standard LaB_6 and CeO_2 samples. The collected 2D diffraction images were integrated and converted to intensity *versus* 2θ using the FIT2D program.[45] The crystallographic parameters were determined by the Rietveld method,[46] using the Fullprof Suite program.[47] Scanning electron microscopy was performed using FESEM from Oxford Instruments attached with EDS. The XPS spectra of the as-prepared samples were recorded with a Thermo Fischer Scientific Multilab 2000 spectrometer using non-monochromatic AlK_α radiation (1486.6 eV) as an X-ray source operated at 150 W (12 kV, 12.5 mA) under ultrahigh vacuum.

2.3 Electrochemical experiments

Electrochemical tests using organic electrolytes were carried out in Swagelok™/coin type cells assembled in an argon-filled glove box. The working electrodes were prepared by mixing the $Na_{0.67}Mn_xCo_{1-x}O_2$ sample, SP carbon and polyvinylidene fluoride (PVDF) binder in the weight ratio of 75 : 20 : 5 with the *N*-ethyl pyrrolidone (NEP) solvent, to form a slurry. The homogenized slurry was coated onto the aluminium foil using a doctor blade. The coated film was dried in a vacuum oven at 80 °C overnight. After calendaring, the film was punched into discs for assembling Na cells. The sodium electrode was prepared by pressing a small piece of sodium metal onto a thin stainless disc. The electrolyte solution was 1 mol L^{-1} $NaPF_6$ dissolved in a mixture of 1 : 1 volume percent of ethylene carbonate–propylene carbonate. A porous glass microfiber filter (Whatman) was used as a separator. The typical sample loading was about 4–5 mg cm^{-2}. The cell thus fabricated was cycled galvanostatically in the voltage range of 1.5 V to 4.2 V *versus* sodium. Cyclic voltammetry experiments were performed with IR compensation. Electrochemical impedance spectroscopy was carried out in the frequency range of 400 kHz to 10 mHz. All the electrochemical experiments were conducted at ambient temperature (303 K) using a VMP3Z Biologic multi-channel potentiostat/galvanostat.

3. Results and discussion

3.1 Crystal structure and morphological analysis

The typical structure of P2 $Na_{0.67}Mn_xCo_{1-x}O_2$ is shown in Fig. 1a. The transition metals, cobalt, and manganese constitute the MO_2 layer, where Co and Mn are randomly distributed due to the similar ionic radii of Co^{3+} (0.545 Å), Co^{4+} (0.53 Å) and Mn^{4+} (0.53 Å).[27,35] The structure can be represented as alternate MO_2 slabs of edge-shared MO_6 octahedra while Na^+ lies in the interlayer spacing.[13,48] The six coordinated Na^+ in a prismatic geometry exists in an edge and face shared environment as shown in the cross-sectional view of MO_2 slabs along

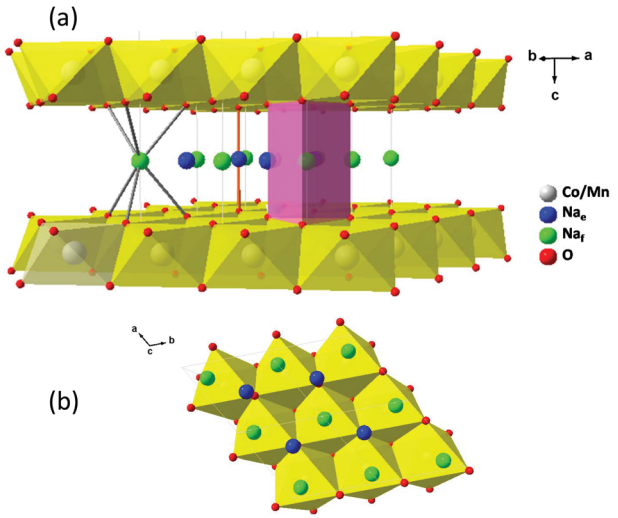

Fig. 1 (a) Crystal structure of layered P2-$Na_{0.67}Mn_xCo_{1-x}O_2$ (x = 0.25, 0.50, 0.75) and (b) structural view along the c-axis highlighting the face and edge sharing Na ions.

the c-axis (Fig. 1b). The green colored Na-ions share the face with metal oxide octahedra above and below, whereas the blue colored Na-ions share the edges. The sodium-ion distribution in these sites strongly depends on the sodium content, the competition between Na^+–$M^{n+/n+1}$ and in-plane Na^+–Na^+ electrostatic repulsions.[37,48]

The powder X-ray diffraction (XRD) pattern of P2-$Na_{0.67}Mn_xCo_{1-x}O_2$ is presented in Fig. 2a–c. All the peaks could be indexed to a hexagonal system with the space group $P6_3/mmc$. The XRD pattern is well consistent with P2-type $Na_{0.67}MnO_2$ (JCPDS No 27-0731)[41] and $Na_{0.71}Co_{0.96}O_2$ (JCPDS File No. 30-1182).[49] As the cobalt content is increased, the base peak (002) shifts towards a higher angle due to the decrease in cell dimensions and the contraction of MO_6 octahedra [Fig. S1, ESI†]. The corresponding lattice parameters and lattice angles obtained by the Rietveld fit and the crystallographic parameters of P2 $Na_{0.67}Mn_xCo_{1-x}O_2$ are presented in Table S2, ESI.† The increase in the Co content decreases the lattice parameters 'a' and 'c' causing the shrinkage of the cell volume and the contraction of Na–O and M–O bonds as shown in Table S2, ESI.† This trend is expected as the more electronegative cobalt (1.9 *versus* 1.5 of that of manganese in the Pauling scale) makes Co–O bonds less ionic, dissipates a negative charge from oxygen and lowers the coulombic/electrostatic repulsion between the MO_2 layers.[27,35] Undoped $Na_{0.67}MnO_2$ prepared by a similar method indicates severe Jahn–Teller distortion (Table S2 and Fig. S3†) which establishes the positive role of cobalt doping in the structural stabilization of $Na_{0.67}MnO_2$.

The FESEM images of P2-$Na_{0.67}Mn_xCo_{1-x}O_2$ are presented in Fig. 3 and Fig. S4, ESI.† The micrograph shows polyhedral crystallites with a mostly hexagonal shape and a particle size of 1–2 μm. EDX mapping confirms the homogeneous distribution of the elements throughout the sample and the estimated composition is closer to the nominal stoichiometry of the phase.

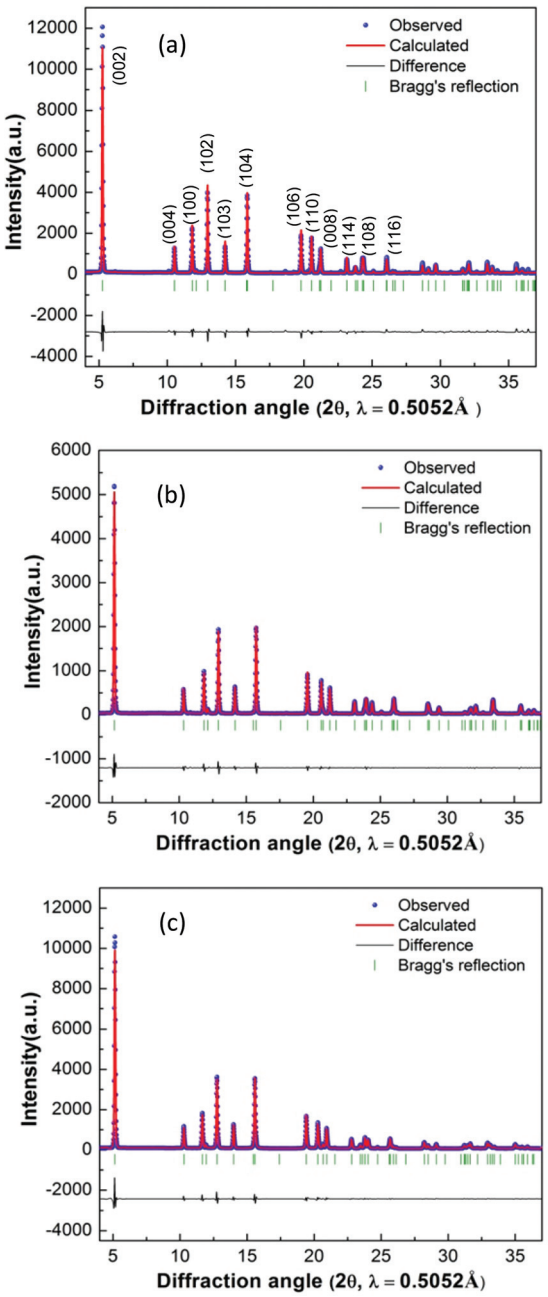

Fig. 2 Rietveld fit for the XRD pattern of (a) $Na_{0.67}Mn_{0.25}Co_{0.75}O_2$, (b) $Na_{0.67}Mn_{0.5}Co_{0.5}O_2$ and (c) $Na_{0.67}Mn_{0.75}Co_{0.25}O_2$. The experimental diffraction pattern (blue dots), the calculated pattern (red line), the difference plot (black line) and the Bragg's diffraction reflections (green ticks) are presented.

The X-ray photoelectron spectroscopy (XPS) spectra of $Na_{0.67}Mn_xCo_{1-x}O_2$ were recorded to ascertain the chemical state of constituent elements. Survey spectra are presented in the ESI (Fig. S5†) which show representative peaks corresponding to Na, Mn, Co, O and C at 1071, 641, 779, 530 and 285 eV, respectively. Adventitious C 1s was observed at 284.5

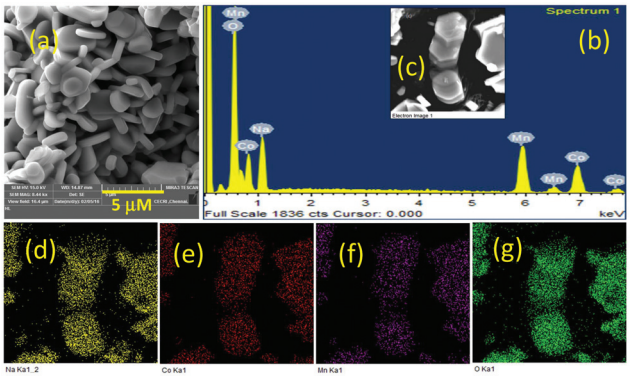

Fig. 3 (a) FESEM image, (b) EDS profile, (c) the image used for elemental mapping, and the homogeneous distribution of (d) sodium (e) cobalt (f) manganese and (g) oxygen of $Na_{0.67}Mn_{0.5}Co_{0.5}O_2$ are presented.

eV and all binding energies could be referenced to this value.[50] Further discussion on C 1s, O 1s and Na 1s spectra is presented in the ESI (Fig. S5† and discussion therein).

As shown in Fig. 4, 1A–3A, cobalt 2p has two peaks with the binding energies of 779 and 794 eV corresponding to $2p_{3/2}$ and $2p_{1/2}$, respectively. The Mn ($2p_{3/2,1/2}$) peaks are observed at 642 and 654 eV (Fig. 4, 1B–3B). Using the curve fitting models reported by Biesinger *et al.* and Nesbitt *et al.*, the core energies of Co and Mn were analyzed.[51,52] In $Na_{0.67}Mn_xCo_{1-x}O_2$, the oxidation state of Mn and Co varies between +3 and +4. Table S6, ESI,† compiles the results of Mn 2p and Co 2p peak fit. In the case of MC50 and MC75, the Mn 2p peak deconvolutes into two predominant peaks; each peak can be further de-convoluted into five peaks.[52] The set of peaks with pink fill corresponds to Mn^{3+} and the other set with yellow fill corresponds to Mn^{4+}. In MC50, the peak areas are in the ratio of about 35 : 65 (Theoretical Value T.V. – Mn^{3+} : Mn^{4+} 34% : 66%) and in MC75, the relative peak areas are in the ratio of 58 : 42% (T.V.: 56 : 44%). In the case of MC25, the $Mn_{(3/2)}$ peak at 642.6 eV can be deconvoluted into five peaks that predicts the presence of manganese only in the tetravalent state. In the same phase, the Co $2p_{3/2}$ peak can be deconvoluted into three peaks at 779.9, 780.9 and 782.26 eV with a prominent shoulder at 789.5 eV indicating the presence of trivalent cobalt.[51,53] Additional peak at 785.2 eV clearly establishes the presence of tetravalent cobalt. The relative areas of Co^{3+} : Co^{4+} regions are in line with their theoretical values of 88 : 12%. In the case of MC50 and MC75, the Co 2p spectrum shows three components at 780.1, 781.4 and 783.2 eV and a satellite peak at 789.2 eV, confirming the presence of cobalt only in the trivalent state.[54] XPS analysis shows that the chemical state of cobalt and manganese and their composition in $Na_{0.67}Mn_xCo_{1-x}O_2$ are in line with their theoretical values (as listed in Table S6, ESI†). Moreover, the redox peaks observed in CV are well correlated with the oxidation states as evidenced from the XPS which is discussed in the later section.

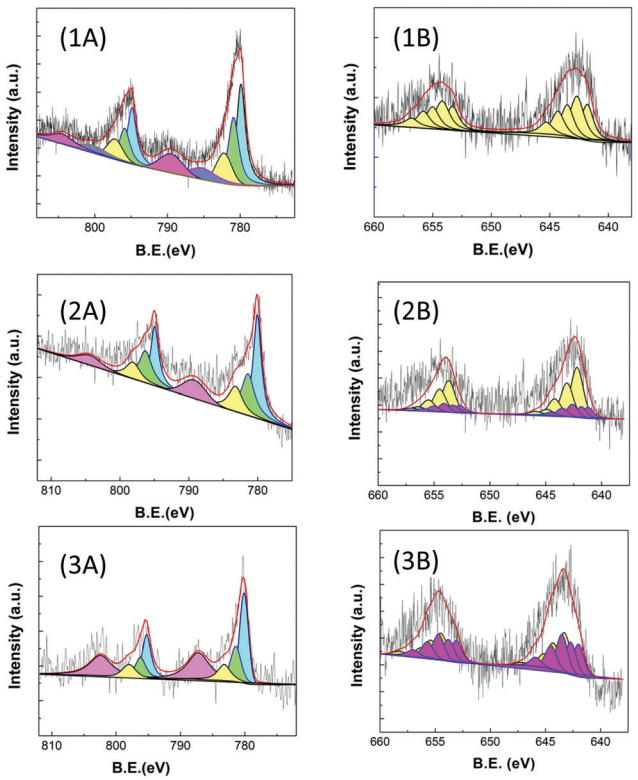

Fig. 4 XPS spectra of (A) manganese and (B) cobalt are shown for (1) $Na_{0.67}Mn_{0.25}Co_{0.75}O_2$, (2) $Na_{0.67}Mn_{0.5}Co_{0.5}O_2$ and (3) $Na_{0.67}Mn_{0.75}Co_{0.25}O_2$.

3.2 Electrochemical properties

Cyclic voltammetry, impedance spectroscopy, and galvanostatic charge–discharge tests were carried out with sodium half-cells of $Na_{0.67}Mn_xCo_{1-x}O_2$ to evaluate their electrochemical Na-ion storage properties. Cyclic voltammetry was carried out for MC25, MC50 and MC75 in the voltage range of 1.5–4.2 V at a scan rate of 0.05 mV s^{-1} and the results are presented in Fig. 5. MC25 shows three sharp oxidation peaks at 3.4 (x), 3.69 (y) and 4.02 V (z) and the corresponding reduction peaks at 3.34 (x′), 3.63 (y′) and 3.98 V (z′). MC50 shows two oxidation peaks at around 1.79 (a) and 4.04 V (z) and the respective reduction peaks at 1.59 (a′) and 4.01 V (z′). MC75 shows oxidation peaks at around 2.0 (a) and 2.2 V (b) and the corresponding reduction peaks at 1.79 (a′) and 2.01 V (b′). Consecutive cyclic voltammograms overlap with each other describing the high stability and the excellent reversibility of the Na-insertion cathodes. A pair of reversible peaks observed in the lower voltage region (~2 V) is associated with the Mn^{4+}/Mn^{3+} redox[55,56] and the minor peaks from 2 to 3 V represent the structural rearrangement of the layers.[18,57] Prominent redox peaks observed at around 3–4 V correspond to the Co^{3+}/Co^{4+} redox[38] and Na^+/vacancy ordering process.[54] Cyclic voltammetry confirms that the charge capacity originates from Co^{3+}/Co^{4+} and Mn^{3+}/Mn^{4+} redox couples, while part of the Mn remains in the tetravalent state. During subsequent discharge, the Co^{4+} ions are reduced to Co^{3+}/Co^{2+} and some of the Mn^{4+} ions are activated below 2 V.[38,55,56,59]

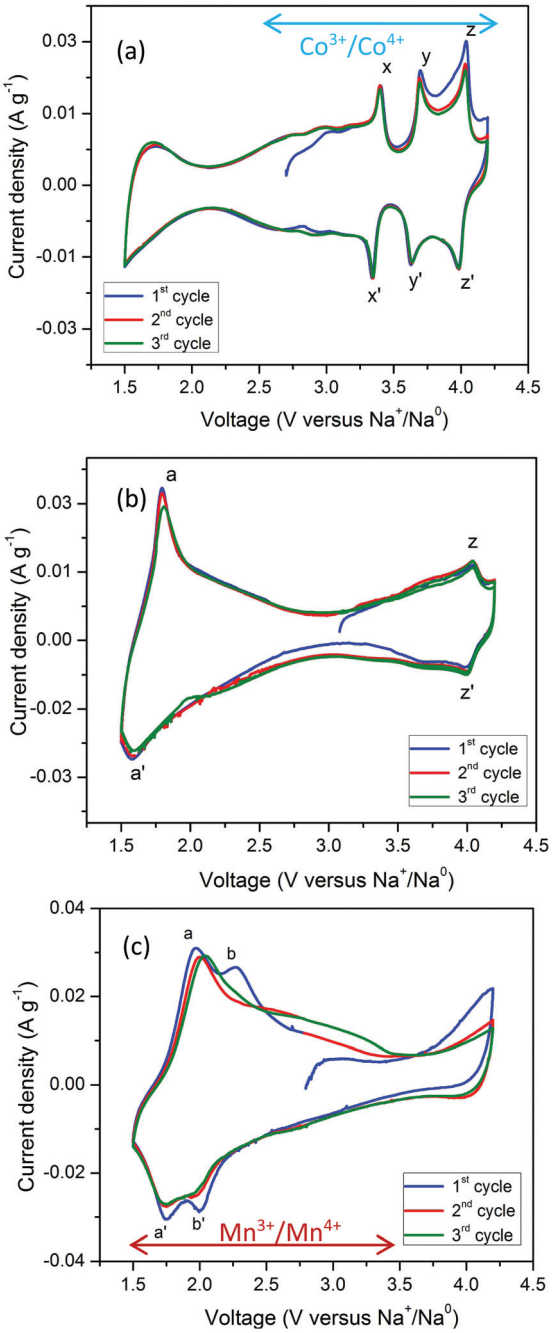

Fig. 5 Cyclic voltammetry plot of (a) $Na_{0.67}Mn_{0.25}Co_{0.75}O_2$, (b) $Na_{0.67}Mn_{0.5}Co_{0.5}O_2$ and (c) $Na_{0.67}Mn_{0.75}Co_{0.25}O_2$ at a scan rate of 0.05 mv s^{-1}.

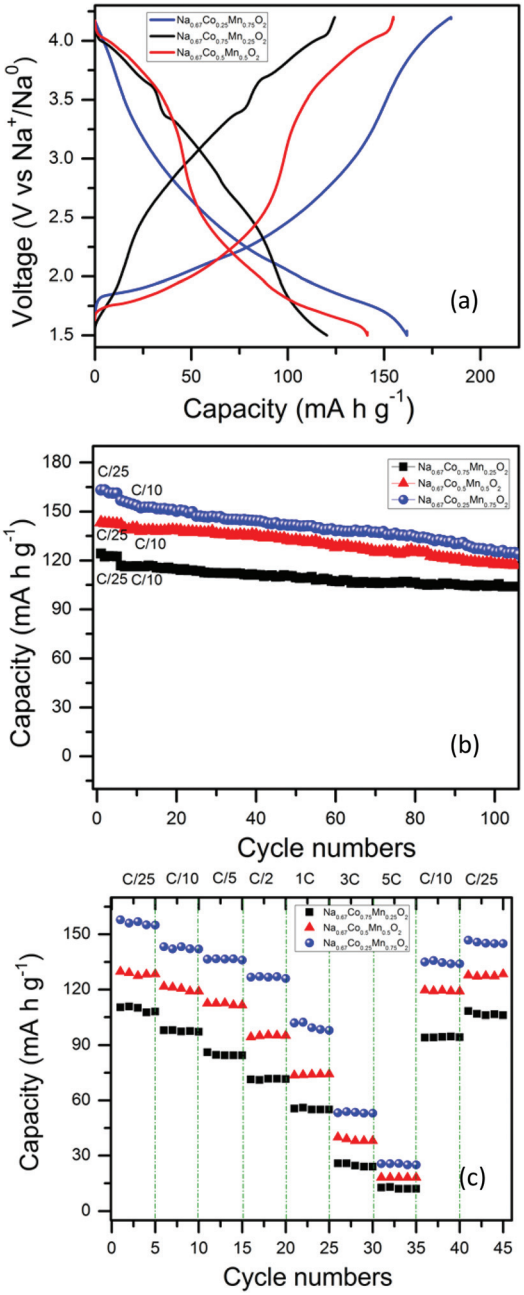

Fig. 6 (a) Cycling plot showing the specific capacity and average potential used for energy calculation. (b) Capacity retention plot and (c) rate capability plot of (1) $Na_{0.67}Mn_{0.25}Co_{0.75}O_2$, (2) $Na_{0.67}Mn_{0.5}Co_{0.5}O_2$ and (3) $Na_{0.67}Mn_{0.75}Co_{0.25}O_2$.

Fig. 6a shows the galvanostatic charge–discharge experiments for three samples carried out in the voltage range of 1.5–4.2 V at C/25 rate (insertion/de-insertion of 1 Na per formula unit in 25 h). According to previous reports, the cycling profiles of the parent compounds, $Na_{0.67}CoO_2$, and $Na_{0.67}MnO_2$, show multiple plateaus.[22,48] However, all the three solid solutions, MC25, MC50 and MC75, depict smooth cycling profiles. The compositions MC50 and MC75 deliver a discharge capacity of about 145 and 167 mA h g^{-1} corresponding to 0.56 and 0.64 moles of sodium, respectively. The Co-rich phase, MC25, exhibits a discharge capacity of about 120 mA h g^{-1} corresponding to the removal of 0.46 moles of Na and the cycling profile shows a sharp potential jump (3.3–3.5 V) on reaching the composition $Na_{0.5}Mn_{0.25}Co_{0.75}O_2$ which is isostructural with orthorhombic $Na_{0.5}CoO_2$. On the other hand, the cycling pattern of MC50 and MC75 shows a sigmoidal *S* type curve and a smooth cycling profile devoid of any potential jump or phase transition driven multiple pla-

teaus. On discharging to 1.5 V, MC50 and MC75 exhibit nominal and over sodiated compositions, $Na_{0.9}Mn_{0.5}Co_{0.5}O_2$ and $Na_{1.05}Mn_{0.75}Co_{0.25}O_2$, respectively. In contrast, the Co-rich phase reaches the chemical composition $Na_{0.7}Mn_{0.25}Co_{0.75}O_2$ at 1.5 V. With an increase in Mn-concentration, higher sodiation is observed during discharge. This arises due to higher oxygen uptake in the as-prepared MC75 [27] which is confirmed by oxygen estimation experiments (Table S7, ESI†). The dQ/dV plots of all the phases clearly establish the reversible phase transitions (Fig. S8, ESI†).

In $Na_{0.67}Mn_xCo_{1-x}O_2$, there are two redox centres corresponding to cobalt and manganese. In the voltage range of the present study, 1.5–4.2 V (*vs.* Na^+/Na), a single redox couple, Co^{3+}/Co^{4+}, is active at around 3–4 V, whereas manganese exhibits two redox couples Mn^{2+}/Mn^{3+} and Mn^{3+}/Mn^{4+}.[27] While the $Mn^{3+/4+}$ redox operates between 2 and 3.5 V, the $Mn^{2+/3+}$ couple becomes active at voltages <2.0 V and can contribute to significant capacity, as much as 45 mA h g^{-1}, and is widely witnessed as a smooth long cycling curve.[27,54] Due to the inductive effect between cobalt and manganese, the extent of substitution shifts the redox voltage of other elements by several hundred mVs; the higher substitution of cobalt pushes the $Mn^{3+/4+}$ redox to lower potential, whereas a higher manganese concentration lifts the $Co^{3+/4+}$ redox to higher potential.[27] Although the presence of divalent cobalt at lower voltages is reported by some groups, the exact active voltage range has not been unambiguously established.[37,38] In other words, the redox voltages of cobalt and manganese are not fixed and vary strongly with their composition.[27]

It is well known that $Na_{0.67}MnO_2$ exhibits discharge capacities of >200 mA g^{-1} but with poor retention. The presence of Jahn–Teller Mn^{3+} reduces the structural stability which is further deteriorated when the oxidation state of the remaining non-trivalent Mn ions converts to 3+ during sodiation/desodiation. In most cases, this is associated with orthorhombic distortion during synthesis or sodium intercalation. The substitution of non-Jahn–Teller ions, even as low as 10%, is expected to mitigate the structural instability and improve the capacity retention.[36] In the present study, the increase in cobalt content in $Na_{0.67}Mn_xCo_{1-x}O_2$ contributes to the capacity retention as part of isovalent Mn^{3+} is replaced, whereas the increase in manganese content contributes to the high specific capacity. X-ray refinement data offers the evidence for the suppression of Jahn–Teller distortion by cobalt substitution. The sodium storage observed in $Na_{0.67}Mn_xCo_{1-x}O_2$ phases is a trade-off between the redox process and mass transport originating from manganese and cobalt.

The Co-rich phases exhibited improved cycling stability as witnessed from the life cycle test. The phases MC25, MC50 and MC75 retained about 91, 87 and 79% of their initial capacities of 107, 121 and 126 mA h g^{-1}, respectively, at the end of 100 cycles with minimum polarization (Fig. 6b). The rate performances of these cathodes were performed at the different current densities from 0.025 A g^{-1} (C/25) to 1.25 A g^{-1} (5C) and are presented in Fig. 6c. MC25 could deliver 90, 75 and 62 mA h g^{-1} at C/5, C/2 and at 1C rate, respectively, whereas MC50 and MC75 delivers 110, 100 and 78 mA h g^{-1}, and 140, 135 and 105 mA h g^{-1} at C/5, C/2 and at 1C rate, respectively. Table S9, ESI,† shows a summary of the literature of P2-$Na_{0.67}Mn_xCo_{1-x}O_2$ cathodes.

3.3 Diffusion coefficient from cyclic voltammetry and impedance spectroscopy

The electrochemical performance of the intercalation electrodes is closely associated with the mass transport of the alkali ion into the bulk of the electrode material. The larger ionic radius of the Na^+ ion (1.12 Å) in comparison with Li^+ (0.76 Å) could hamper sodium diffusion leading to an inferior performance of Na-insertion electrodes compared to their Li-counterparts. Therefore, it is important to estimate the D_{Na^+} values to comprehend the electrode performance. Electrochemical techniques such as cyclic voltammetry (CV), electrochemical impedance spectroscopy (EIS), galvanostatic intermittent titration technique (GITT), potentiostatic intermittent titration technique (PITT) have been employed to estimate the chemical diffusion coefficient of Li^+/Na^+ in insertion electrodes.[58–61]

CV and EIS techniques were used to calculate the apparent chemical diffusion coefficient of Na^+ in $Na_{0.67}Mn_xCo_{1-x}O_2$ series. The diffusion coefficients are derived from the slope obtained from the linear fit of plotting i_p *vs.* $\upsilon^{1/2}$. For comparison, it is also deduced from the Warburg impedance measured by stopping the cell at specific peak potentials and from the peak current contributing to the Co and Mn redox. The fundamental rationale is to estimate D_{Na^+} at specific potentials corresponding to the Co^{3+}/Co^{4+} (above 3 V) or Mn^{3+}/Mn^{4+} (below 3 V) redox. During the charge/discharge process, changes in the stoichiometry of Na^+, the oxidation state of Co/Mn and the resulting structural changes will influence D_{Na^+} and it is imperative to understand the relation between these driving forces and mass transport.

The approach presented here is not infallible and has some limitations. First, diffusion in an electrolyte and in a solid electrode film is a different phenomenon and the electrochemical approach accorded to them must also be different. The classical Randles–Sevcik equation primarily concerns with ionic diffusion in electrolytes and therefore the i_p *vs.* $\upsilon^{1/2}$ plot for $Na_{0.67}Mn_xCo_{1-x}O_2$ presented here is an approximate method to estimate the diffusion coefficient of Na^+. Hence, the results presented here offer only a qualitative picture of diffusion coefficient, thereby aiding us to compare the effect of Co doping in $Na_{0.67}MnO_2$. Second, the capacitive effect of added conductive carbon cannot be ignored. To minimize the capacitive charge storage originating from SP carbon, and the electrode materials at higher scan rates, the domain of 0.2–1 mV s^{-1} is used in the present study.[58]

CV experiments were conducted at various scan rates in the range of 0.2 to 1 mV s^{-1} on MC25, MC50 and MC75 half-cells (Fig. S10, ESI†) to obtain Na-ion diffusion. The increase in peak currents with the scan rate and farther divergence of cathodic–anodic peaks are observed for all the compositions.

According to the Randles–Sevcik equation, the peak current (i_p) is proportional to the square root of scan rate ($v^{1/2}$),

$$i_p = 2.69 \times 10^5 An^{3/2} CD^{1/2} v^{1/2} \quad (1)$$

On rearranging eqn (1) and substituting slope (m) = $i_p/v^{1/2}$

$$D = [\text{slope } (m)/(2.69 \times 10^5 An^{3/2} C)]^2 \quad (2)$$

where i_p is the peak current (A), F is Faraday's constant (96 485 C mol^{-1}), A is the surface area of the active material in the electrode (cm^2), n is the number of electrons per molecule during oxidation/reduction, C is the concentration of sodium ions (mol cm^{-3}), D_{Na} is the diffusion coefficient (cm^2 s^{-1}), and v is the scan rate (V s^{-1}). The slope (m) for oxidation and reduction can be obtained from the linear fit on plotting the peak current (i_p) *versus* square root of scan rate (v) as shown in Fig. S11, ESI.† From Table S13, ESI,† the diffusion coefficient for oxidation and reduction reactions in the case of MC25 (8.6×10^{-9} cm^2 s^{-1}, 5.5×10^{-9} cm^2 s^{-1}, respectively) is comparatively higher than that ofMC75 (4.4×10^{-9} cm^2 s^{-1}, 5×10^{-9} cm^2 s^{-1}, respectively).

In addition, cyclic voltammograms for the three compositions at a scan rate of 0.05 mV s^{-1} were recorded (Fig. 5). The diffusion coefficients are calculated from the peak current using eqn (1). From Table S13, ESI,† the diffusion coefficient calculated for the redox couple above 3 V corresponding to cobalt (MC25 $\sim 10^{-10}$ cm^2 s^{-1}) is relatively higher than the diffusion coefficient calculated for the redox couple below 3 V corresponding to manganese (MC75 $\sim 10^{-11}$ cm^2 s^{-1}). It is evident from the CV measurements that the diffusion of sodium ions is more pronounced in the Co-rich phase than in the Mn-rich phase. In order to corroborate the diffusion coefficient from CV, EIS measurements were also carried out.

Electrochemical impedance spectroscopy (EIS) experiments were performed on MC25, MC50 and MC75. Two different EIS experiments were carried out to study the kinetics. First, EIS experiments were recorded on a fresh cell and at the end of the first charge, first discharge and fifth discharge for the three compositions (Fig. 7, Fig. S12 and Table S13, ESI†). Another set of EIS was recorded on cells at different peak potentials associated with the manganese and cobalt redox observed below and above 3 V, respectively (Fig. S14, S15 and Table S16, ESI†).

The Nyquist plot shows a semicircle in the high to mid frequency region and a sloping line in the low-frequency region. The shift from the origin represents the internal/ohmic resistance/solution resistance of the cell (R_s). The semicircle represents the Na-ion migration through the interface: between the surface of the electrode and the electrolyte. The charge-transfer resistance also represents the electronic conductivity of the material which is approximately equal to the diameter of the semicircle on the Z_{real} (Z') axis, in the high-frequency region which is a parallel combination of a capacitor (C_{dl}) and a resistor (R_{ct}). The straight line at an angle of 45° with respect to the horizontal axis (Z_{real}) is attributed to the semi-infinite diffusion while the divergent spectrum contributes to the finite diffusion. The R_s values for all the impedance measurements were closer to 20 ohms (Fig. 7). The R_{ct} values systematically increased from a fresh cell to the fifth discharge which may be attributed to the formation of the passivating SEI film in the initial cycles. The values of R_{ct} for the first and fifth discharge of the Co-rich phase (MC25) were 600 and 900 Ω, respectively (Fig. 7a). On the other hand, the Mn-rich phase (MC75) showed the R_{ct} values of about 2500 and 4500 Ω in the first and fifth discharge, respectively (Fig. 7c). The R_{ct} values of the Co-rich phase are comparatively lower than those of the

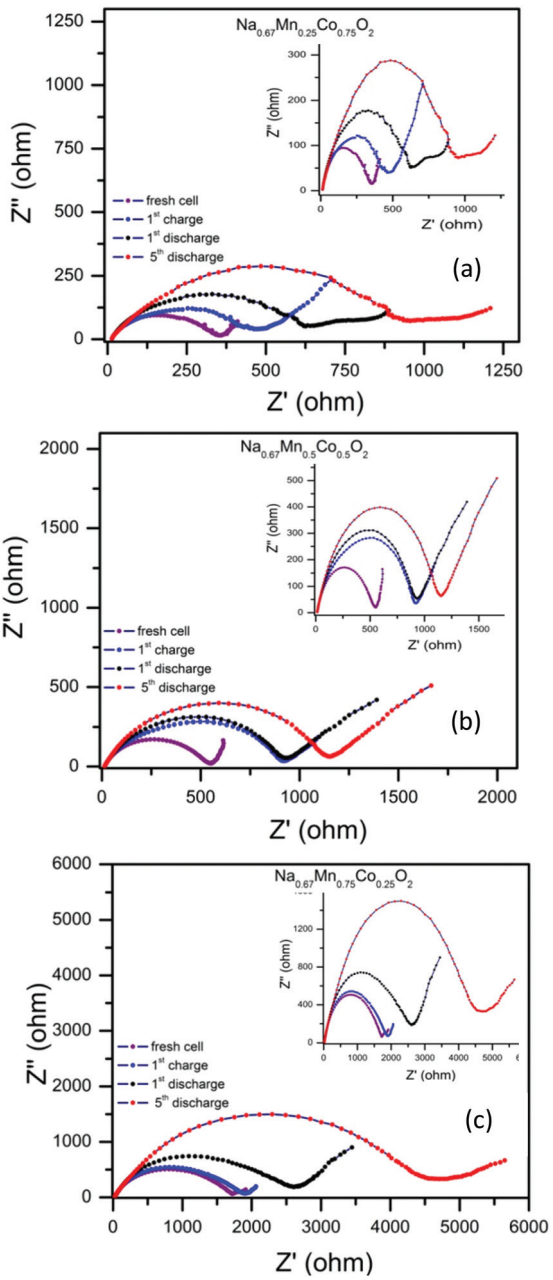

Fig. 7 Nyquist plots of the fresh cell, first charge, first and fifth discharge of (a) $Na_{0.67}Mn_{0.25}Co_{0.75}O_2$, (b) $Na_{0.67}Mn_{0.5}Co_{0.5}O_2$ and (c) $Na_{0.67}Mn_{0.75}Co_{0.25}O_2$.

Mn-rich phase. It is evident from the R_{ct} values that the electronic conductivity of the cathode material increases with the increase in cobalt content.

The sloping line in the low-frequency region depicts the Na-ion diffusion into the bulk of the electrode material. The sodium-ion diffusion coefficient (D_{Na} in $cm^2\ s^{-1}$) can be calculated using the following equation:

$$D = R^2T^2/2A^2n^4F^4C^2\sigma^2 \quad (3)$$

$$Z' = R_s + R_{ct} + \sigma\omega^{-1/2} \quad (4)$$

where R is the gas constant (8.314 J mol^{-1} K^{-1}), T is the absolute temperature (298 K), A is the surface area of the electrode (cm^2), n is the number of electrons per molecule during oxidation/reduction, F is Faraday's constant (96 485 C mol^{-1}), C is the concentration of sodium ions (mol cm^{-3}) which could be calculated from the density (ρ in g cm^{-3}) and molecular weight (M in g mol^{-1}), and σ is the Warburg factor (ohm $s^{-1/2}$) which is determined from the slope of the curve obtained by plotting the square root of frequency (ω in sec) on the x-axis and Z_{real} (Z' in ohm) on the y-axis (Fig. S12 and S15, ESI†). The intercept value corresponds to the electrolyte resistance and charge-transfer resistance ($R_s + R_{ct}$ in ohm) values. These values are in concordant with the R_{ct} values calculated from the diameter of the semicircle in the high-frequency region and are already discussed in the previous section.

The diffusion coefficient calculated after the first and fifth discharge of MC25 (10^{-11} cm^2 s^{-1}) is relatively higher than that of MC75 (10^{-13} cm^2 s^{-1}), whereas MC50 (10^{-12} cm^2 s^{-1}) holds the intermediate value (Table S13, ESI†). The diffusion coefficient calculated from the EIS measured at different peak potentials shows that the potentials corresponding to cobalt (~10^{-11} to 10^{-12} cm^2 s^{-1}) exhibit a higher diffusion coefficient than the potentials corresponding to the manganese redox (~10^{-12} to 10^{-13} cm^2 s^{-1}) (Fig. S14, S15 and Table S16, ESI†).

Diffusion coefficients calculated from the CV and EIS measurements for the solid solution $Na_{0.67}Mn_xCo_{1-x}O_2$ were in the range of 10^{-9} to 10^{-13} cm^2 s^{-1} which are higher than the diffusion coefficient reported for $Na_{0.67}MnO_2$ (10^{-14} cm^2 s^{-1}).[21] Furthermore, among the three compositions studied here, the calculated Na^+ diffusion coefficient value is higher in the sample containing a higher cobalt content (MC25). It is observed that the rate performance is similar for all the three compositions although the calculated diffusion coefficients were different. In other words, solid state diffusion is not rate limiting, which is not unexpected with the small particle size. As XPS data points out, phases with significant manganese concentrations such as MC50 and MC75 contain Jahn–Teller Mn^{3+} ions forming high-spin complexes which lower the structural stability. As a result in the solid solutions $Na_{0.67}Mn_xCo_{1-x}O_2$, the increase in cobalt content contributes to the capacity retention replacing part of isovalent Mn^{3+}, whereas the increase in manganese content contributes to the high specific capacity but with inferior retention. Cobalt substitution improves the Na^+ diffusion and also enhances the electronic conductivity. As witnessed from the X-ray diffraction data analysis (Table S2, ESI† and discussion therein), cobalt substitution causes the contraction of MO_6 octahedra and the enlargement of inter-slab 'd' spacing which improves the structural stability during Na^+ intercalation/de-intercalation. In addition, more open space can expedite ionic transport more effectively. As a result, phases containing more cobalt exhibit stable Na-ion storage over longer cycles (Fig. 6b). Hence, the multi-pronged role of cobalt in improving the structural stability and electrochemical performance of $Na_{0.67}Mn_xCo_{1-x}O_2$ is demonstrated through the combination of structural analysis, cyclic voltammetry, impedance spectroscopy and electrochemical Na-ion storage.

4. Conclusions

P2-$Na_{0.67}Mn_xCo_{1-x}O_2$ (x = 0.25, 0.5, 0.75) were investigated as cathode materials for Na-ion batteries to comprehend the pivotal role of cobalt in supporting the structural integrity and Na-ion diffusion. Sodium-ion diffusion coefficients (D_{Na^+}) in these solid solutions were in the range of 10^{-11} to 10^{-13} cm^2 s^{-1}. Higher diffusion coefficient values were observed in the voltage domain of Co^{3+}/Co^{4+} redox, and D_{Na^+} values increased with the increase in cobalt content in the order MC25 > MC50 > MC75. The structural stability and capacity retention followed a similar trend, while the discharge capacity values followed the reverse order. The observed D_{Na^+} values could be correlated to the analogous contraction in Co/Mn–O bond lengths and the increase in inter-slab distance which provides more room for Na-ion diffusion. The capacity retention with the increase in cobalt content is due to the better structural stability attributed to the suppressed Jahn–Teller effect.

Conflicts of interest

The authors claim no competing financial interest.

Acknowledgements

Ms K. Hemalatha thanks the Council of Scientific and Industrial Research (CSIR) for granting a Senior Research Fellowship. This work was supported by the Department of Science and Technology-Science and Engineering research board, New Delhi, under the grant scheme "Clean Energy Research Initiative" (Grant No. DST/TMD/CERI/C16). The authors would like to acknowledge the help of Dr V. Srihari and staff at Extreme conditions ED/AD-XRD Beam line (BL-11), Indus-2 for synchrotron X-ray diffraction measurements.

References

1 J. M. Tarascon and M. Armand, *Nature*, 2001, **414**, 359–367.
2 M. Armand and J. M. Tarascon, *Nature*, 2008, **451**, 652–657.

3 V. Palomares, M. C. Cabanas, E. C. Martinez, M. H. Han and T. Rojo, *Energy Environ. Sci.*, 2013, **6**, 2312–2337.
4 D. Kundu, E. Talaie, V. Duffort and L. F. Nazar, *Angew. Chem., Int. Ed.*, 2015, **54**, 2–20.
5 M. D. Slater, D. Kim, E. Lee and C. S. Johnson, *Adv. Funct. Mater.*, 2013, **23**, 947–958.
6 http://en.wikipedia.org/wiki/Abundance of the chemical elements; R. S. Carmichael, *Practical Handbook of physical properties of Rocks and Minerals*, CRC Press, Boca Raton, FL, 1989; D. R. Lide, *Handbook of Chemistry and Physics, Special Student Edition*, CRC Press, 77th edn, 1996.
7 S. W. Kim, D. H. Seo, X. Ma, G. Ceder and K. Kang, *Adv. Energy Mater.*, 2012, **2**, 710–721.
8 H. Pan, Y.-S. Hu and L. Chen, *Energy Environ. Sci.*, 2013, **6**, 2338–2360.
9 N. Yabuuchi, K. Kubota, M. Dahbi and S. Komaba, *Chem. Rev.*, 2014, **114**, 11636–11682.
10 K. Kubota and S. Komaba, *J. Electrochem. Soc.*, 2015, **162**, A2538–A2550.
11 M. H. Han, E. Gonzalo, G. Singh and T. Rojo, *Energy Environ. Sci.*, 2015, **8**, 81–102.
12 K. Kubota, N. Yabuuchi, H. Yoshida, M. Dahbi and S. Komaba, *Mater. Res. Bull.*, 2014, **39**, 416–422.
13 Y. Mo, S. P. Ong and G. Ceder, *Chem. Mater.*, 2014, **26**, 5208–5214.
14 L. W. Shacklette, T. R. Jow and L. Townsend, *J. Electrochem. Soc.*, 1988, **135**, 2669–2674.
15 X. H. Ma, H. L. Chen and G. Ceder, *J. Electrochem. Soc.*, 2011, **158**, A1307–A1312.
16 D. Su, C. Wang, H.-J. Ahn and G. Wang, *Chem. – Eur. J.*, 2013, **19**, 10884–10889.
17 N. Yabuuchi, M. Kajiyama, J. Iwatate, H. Nishikawa, S. Hitomi, R. Okuyama, R. Usui, Y. Yamada and S. Komaba, *Nat. Mater.*, 2012, **11**, 512–517.
18 C. Delmas, C. Fouassier and P. Hagenmuller, *Physica B+C*, 1980, **99**, 81–85.
19 J. P. Parant, R. Olazcuaga, M. Devalette, C. Fouassier and P. Hagenmuller, *J. Solid State Chem.*, 1971, **3**, 1–11.
20 R. J. Clement, P. G. Bruce and C. P. Grey, *J. Electrochem. Soc.*, 2015, **162**, 14.
21 A. Mendibourne, C. Delmas and P. Hagenmuller, *J. Solid State Chem.*, 1985, **57**, 323–331.
22 A. Caballero, L. Hernan, J. Morales, L. Sanchez, J. Santos Pena and M. A. G. Aranda, *J. Mater. Chem.*, 2002, **12**, 1142–1147.
23 N. Bucher, S. Hartung, A. Nagasubramaniam, Y. L. Cheah, H. E. Hoster and S. Madhavi, *ACS Appl. Mater. Interfaces*, 2014, **6**, 8059–8065.
24 R. Stoyanova, D. Carlier, M. Sendova-vassileva, M. Yoncheva, E. Zhecheva, D. Nihtianova and C. Delmas, *J. Solid State Chem.*, 2010, **183**, 1372–1379.
25 M. Yoncheva, R. Stoyanova, E. Zhecheva, E. Kuzmanova, M. Sendova-vassileva, D. Nihtianova, D. Carlier, M. Guignard and C. Delmas, *J. Mater. Chem. A*, 2012, **22**, 23418–23427.
26 M. Dolle, S. Patoux and M. M. Doeff, *Chem. Mater.*, 2005, **17**, 1036–1043.
27 X. Wang, M. Tamaru, M. Okubo and A. Yamada, *J. Phys. Chem. C*, 2013, **117**, 15545–15551.
28 J. S. Thorne, R. A. Dunlap and M. N. Obravac, *J. Electrochem. Soc.*, 2013, **160**, A361–A367.
29 B. M. Boisse, D. Carlier, M. Guignard, L. Bourgeois and C. Delmas, *Inorg. Chem.*, 2014, **53**, 11197–11205.
30 J. M. Paulsen and J. R. Dahn, *Solid State Ionics*, 1999, **126**, 3–24.
31 L. Bordet-Le Guenne, P. Deniard, P. Biensan, C. Siret and R. Brec, *J. Mater. Chem. A*, 2000, **10**, 2201–2206.
32 N. Yabuuchi, R. Hara, M. Kajiyama, K. Kubota, T. Ishigaki, A. Hoshikawa and S. Komaba, *Adv. Energy Mater.*, 2014, **4**, 1301453–1301475.
33 J. Billaud, G. Singh, A. Robert Armstrong, E. Gonzalo, V. Roddatis, M. Armand, T. Rojo and P. G. Bruce, *Energy Environ. Sci.*, 2014, **7**, 1387–1391.
34 T. A. Eriksson, Y. J. Lee, J. Hollingsworth, J. A. Reimer, E. J. Cairns, X.-F. Zhang and M. M. Doeff, *Chem. Mater.*, 2003, **15**, 4456–4463.
35 D. Baster, W. Zajac, L. Kondracki, F. Hartman and J. Molenda, *Solid State Ionics*, 2016, **288**, 213–218.
36 N. Bucher, S. Hartung, J. B. Franklin, A. M. Wise, L. Y. Lim, H.-Y. Chen, J. N. Weker, M. F. Toney and M. Srinivasan, *Chem. Mater.*, 2016, **28**, 2041–2051.
37 D. Carlier, J. H. Cheng, R. Berthelot, M. Guignard, M. Yoncheva, R. Stoynova, B. J. Hwang and C. Delmas, *Dalton Trans.*, 2011, **40**, 9306–9312.
38 J.-H. Cheng, C.-J. Pan, J.-F. Lee, J.-M. Chen, M. Guignard, C. Delmas, D. Carlier and B. J. Hwang, *Chem. Mater.*, 2014, **26**, 1219–1225.
39 F. R. Beck, Y. Q. Cheng, Z. Bi, M. Feygenson, C. A. Bridges, Z. M. Rosenberg, A. Manthiram, J. B. Good enough, M. P. Paranthaman and A. Manivannan, *J. Electrochem. Soc.*, 2014, **161**, A961–A967.
40 Y.-E. Zhu, X. Qi, X. Chen, X. Zhou, X. Zhang, J. Wei, Y. Hu and Z. Zhou, *J. Mater. Chem. A*, 2016, **4**, 11103–11109.
41 X. Xu, S. Ji, R. Gao and J. Liu, *RSC Adv.*, 2015, **5**, 51454–51460.
42 N. Bucher, S. Hartung, I. Gocheva, Y. L. Cheah, M. Srinivasan and H. E. Hoster, *J. Solid State Electrochem.*, 2013, **17**, 1923–1929.
43 K. R. Prakash and A. S. Prakash, *RSC Adv.*, 2015, **5**, 94411–94417.
44 K. Pandey, H. Poswal, A. Mishra, A. Dwivedi, R. Vasanthi, N. Garg and S. M. Sharma, Energy-dispersive X-ray diffraction beamline at Indus-2 synchrotron source, *Pramana*, 2013, **80**, 607–619.
45 A. P. Hammersley, S. O. Svenson, M. Han and D. Hauserman, *High Pressure Res.*, 1996, **14**, 235–248.
46 H. M. Rietveld, *J. Appl. Crystallogr.*, 1969, **2**, 65–71.
47 J. Rodriguez Carvajal, *Phys. B*, 1993, **192**, 55–69.
48 R. Berthelot, D. Carlier and C. Delmas, *Nat. Mater.*, 2011, **10**, 74–80.

49 M. D. Arienzo, R. Ruffo, R. Scotti, F. Morazzoni, C. M. Mari and S. Polizzi, *Phys. Chem. Chem. Phys.*, 2012, **14**, 5945–5952.
50 R. Dedryvère, D. Foix, S. Franger, S. Patoux, L. Daniel and D. Gonbeau, *J. Phys. Chem. C*, 2010, **114**, 10999–11008.
51 M. C. Biesinger, B. P. Payne, A. P. Grosvenor, L. W. M. Lau, A. R. Gerson and R. Smart, *Appl. Surf. Sci.*, 2011, **257**, 2717–2730.
52 H. W. Nesbitt and D. Banerjee, *Am. Mineral.*, 1998, **83**, 305–315.
53 J. C. Dupin, D. Gonbeau, H. Benqlilou-Moudden, P. Vinatier and A. Levasseur, *Thin Solid Films*, 2001, **384**, 23–32.
54 Z.-Y. Li, R. Gao, L. Sun, Z. Hu and X. Liu, *J. Mater. Chem. A*, 2015, **3**, 16272–16278.
55 K. Hemalatha, M. Jayakumar, P. Bera and A. S. Prakash, *J. Mater. Chem. A*, 2015, **3**, 20908–20912.
56 B.-C. Jang, S.-B. Yang and J.-T. Son, *J. Nanosci. Nanotechnol.*, 2016, **16**, 8347–8351.
57 X. Sun, X.-Y. Ji, H.-Y. Xu, C.-Y. Zhang, Y. Shao, Y. Zhang and C.-H. Chen, *Electrochim. Acta*, 2016, **208**, 142–147.
58 P. Yu, B. N. Popov, J. A. Ritter and R. E. White, *J. Electrochem. Soc.*, 1999, **146**, 8–14.
59 J. Wang, X. Li, Z. Wang, H. Guo, B. Huang, Z. Wang and G. Yan, *J. Solid State Electrochem.*, 2015, **19**, 153–160.
60 M. Zhao, W. Zhang and X. Song, *Dalton Trans.*, 2017, **46**, 3857–3863.
61 S. Li, Y. F. Dong, L. Xu, X. Xu, L. He and L. Mai, *Adv. Mater.*, 2014, **26**, 3545–3553.